Temperature dependence of the giant dipole resonance width in ^{152}Gd

C. Ghosh,[1] G. Mishra,[2] A. K. Rhine Kumar,[1] N. Dokania,[1] V. Nanal,[1,*] R. G. Pillay,[1] Suresh Kumar,[2] P. C. Rout,[2] Sandeep Joshi,[2] and P. Arumugam[3]

[1]*Department of Nuclear and Atomic Physics, Tata Institute of Fundamental Research, Mumbai 400005, India*

[2]*Nuclear Physics Division, Bhabha Atomic Research Centre, Mumbai 400085, India*

[3]*Department of Physics, Indian Institute of Technology, Roorkee 247667, India*

(Received 18 March 2016; published 21 July 2016)

To investigate the dependence of giant dipole resonance (GDR) width on temperature (T) and angular momentum (J), high energy γ-ray spectra were measured in the reaction ^{28}Si + ^{124}Sn at $E_{^{28}\mathrm{Si}} = 135$ MeV. The J information was deduced from multiplicity of low-energy γ rays. The GDR parameters, namely, the centroid energy and width are extracted using statistical model analysis. The observed variation of the GDR width for $T \sim 1.2$–1.37 MeV and $J \sim 20\hbar$–$40\hbar$ is consistent with the universal scaling given by Kusnezov *et al.*, which is applicable in the liquid-drop regime. The GDR input cross sections extracted from the statistical model best fits are compared with thermal shape fluctuation model (TSFM) calculations and are found to be in good agreement. The TSFM calculations predominantly favor the noncollective oblate shape, while the statistical model fit with both prolate and oblate shapes describes the data. The present data together with earlier measurements indicate a very slow variation of the GDR width for $T \sim 1.2$ to 1.5 MeV. The observed trend is well explained by the TSFM calculations, although the calculated values are ∼4%–13% higher than the data.

DOI: 10.1103/PhysRevC.94.014318

I. INTRODUCTION

The isovector giant dipole resonance (GDR) built on excited states of atomic nuclei provides a unique probe to understand the structure of hot and rotating nuclei. The GDR width (Γ) provides insight into the physics of the damping mechanism of the GDR and has been extensively studied for nuclei over a wide mass range [1–3]. Most of the experiments used heavy-ion fusion reactions for populating nuclei at high temperature (T) and angular momentum (J), while in some cases GDR studies at different T were carried out using inelastic reactions [4,5]. The experimentally observed GDR width is a combination of both temperature- and angular-momentum-related effects and they need to be disentangled for a proper understanding of the variation of GDR properties as a function of T and J. A detailed discussion on various factors that contribute to the observed GDR width is given in Refs. [1,6–10]. At lower T, where the nuclear shell structure persists, the effective GDR width is dominated by nuclear structure driven by angular momentum. At high T, the shape of the nucleus fluctuates about an equilibrium shape and these fluctuations also result in broadening of the GDR width.

Different theoretical approaches have been employed to explain the observed broadening of the GDR width in excited nuclei [8,11–13]. The thermal shape fluctuation model (TSFM) is largely successful in describing the T dependence of the GDR width in excited nuclei [8–11]. According to this model, the GDR observables are the result of the ensemble average over the different shapes sampled by the nucleus at finite T. With increasing T, fluctuation around the mean shape increases, thereby resulting in increased effective GDR width. The phenomenological scaling formula (PSF) given by Kusnezov *et al.* [13] introduced the concept of reduced GDR width, which is described by the global function $L(\xi)$ for nuclei in the liquid-drop regime, where $\xi = J/A^{5/6}$ and A is the mass number of the nucleus. Recently, an improved phenomenological scaling formula has been proposed by Pandit *et al.* [14] to explain the systematics of the GDR observables, taking into consideration the GDR-induced intrinsic fluctuation.

The study of GDR in ^{152}Gd [6,15] was motivated by the fact that although the PSF is successful for a range of nuclei, some differences were observed in the $A \sim 150$ region [16]. While the GDR width variation in ^{152}Gd with J was found to agree with the PSF, the effect of collisional damping had to be taken into consideration to explain the observed larger GDR width at higher T (∼1.6 to 1.9 MeV) [6,15]. An alternative explanation was suggested in Ref. [17], where the observed GDR widths for ^{152}Gd were explained using the critical temperature-based formula (henceforth referred to as CTF). In light of recent TSFM calculations [18] in ^{152}Gd in the range of T-J covered in the above references, it has been claimed that the observed GDR width and the GDR cross section cannot be explained in a consistent manner. It should be pointed out that in Ref. [18] the calculations have been compared with a linearized representation of data (obtained by dividing the data with a calculated statistical model spectrum employing an arbitrary $E1$ strength), which is not a proper representation of the GDR strength function. Therefore, to further investigate the T dependence of the GDR width for a similar J range, the GDR studies are carried out in ^{152}Gd at lower T (1.25 to 1.37 MeV), where the effects of collisional damping are expected to be small. In addition, the pre-equilibrium emission and nuclear bremsstrahlung are also expected to be negligible at lower excitation energies.

In this paper, the results of GDR measurement in the ^{152}Gd nucleus at an excitation energy of ∼71 MeV using the

*nanal@tifr.res.in

^{28}Si + ^{124}Sn reaction are presented. The T and J dependence of the GDR width are extracted within the statistical model framework. For a proper comparison with TSFM calculations, the input GDR cross section corresponding to the best-fit statistical model analysis is used. The results are also compared with earlier measurements to understand the GDR width variation over a wider temperature range. The paper is organized as follows: Section II gives the experimental details of the GDR measurements. Section III describes the statistical model analysis to extract the GDR parameters. The comparison of data with those of the TSFM and with those of the phenomenological scaling formulas (PSF and CTF) are discussed in Sec. IV. A summary of results and conclusions is presented in Sec. V.

II. EXPERIMENTAL DETAILS

The experiment was carried out using a pulsed beam of ^{28}Si ($E_{^{28}\mathrm{Si}} = 135$ MeV) from the Pelletron Linac Facility, Mumbai. The target was a ∼2.0 mg/cm^2 (97.20% enriched) thick self-supporting ^{124}Sn foil and the beam energy at the target center was ∼130 MeV. The experimental setup was similar to that described in Ref. [15]. High-energy γ rays were detected in an array of seven close-packed hexagonal BaF_2 detectors (each 20 cm long with a face-to-face distance of 9 cm) surrounded by an annular plastic scintillator shield (5 cm thick, 40 cm long) for cosmic background rejection. In addition, a 5-mm-thick lead sheet was placed in front of the array for attenuating low-energy γ rays and x rays and an ∼10-cm-thick lead shield was placed around the detector array for reducing ambient as well as beam-induced γ-ray background. The BaF_2 array was placed at 125° with respect to the beam direction and at a distance of ∼50 cm from the target center. The neutron-γ ray separation was achieved using time-of-flight (TOF) with respect to the RF pulse. The beam dump was placed downstream at a sufficiently large distance (∼4 m) to minimize the background. Both the beam dump (tantalum) and the upstream collimators (tungsten) were suitably shielded using borated paraffin and lead for stopping the neutrons and γ rays, respectively.

The information of the angular momentum of a compound nucleus (CN) is inferred from the multiplicity of low-energy discrete γ rays. The low-energy γ rays were detected in an array consisting of 36 hexagonal BGO detectors (each 7.6 cm long with a face-to-face distance of 5.6 cm) arranged in a close-packed castle geometry near the target. The multiplicity is deduced from the fold (F), defined as number of BGO detectors recording a signal for $E_\gamma \geqslant 150$ keV within a coincidence window of 50 ns. The efficiency of the multiplicity array (ϵ_M) was measured at $E_\gamma = 662$ keV using ^{137}Cs as the source and found to be ∼54%, which is in good agreement with GEANT3-based simulation ($\epsilon_M^{\mathrm{sim}}$) incorporating the exact detector geometry. Due to the presence of isomers, $\epsilon_M^{\mathrm{sim}}$ was calculated as a function of downstream distance from the target for different energies. The cross-talk probability for BGO detectors was also simulated over a range of energies [15].

Event-by-event data was acquired by a CAMAC-based acquisition system LAMPS [19] for a 0.1 pmC of incident charge. The master trigger was generated for $E_{\mathrm{sum}} > 4$ MeV,

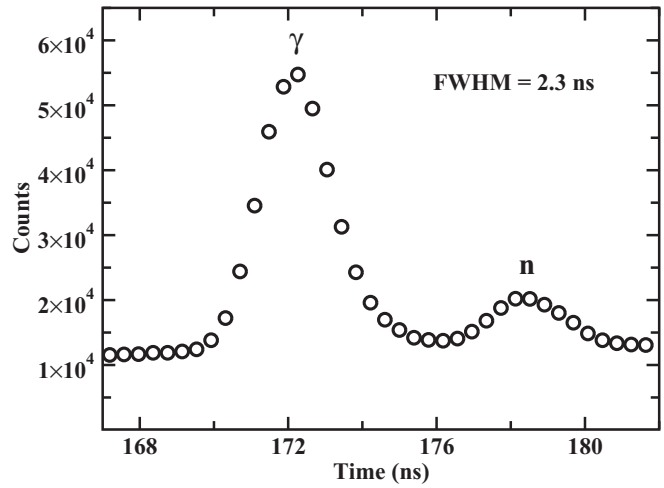

FIG. 1. Typical time-of-flight spectrum for the central BaF_2 detector.

where E_{sum} is the total energy deposited in the BaF_2 detector array. The individual BaF_2 detector anode pulse was integrated in two different gate widths of 200 ns (E_{short}) and 2 μs (E_{long}) for pileup rejection and energy measurements, respectively. For each event, all outputs of individual BaF_2 detectors, namely, E_{short}, E_{long}, and BaF_2-TOF, were recorded together with the fold and the T_{BGO} (time signal for the BGO detector array with respect to the RF pulse).

Energy calibration of the BaF_2 detectors was performed using standard low-energy radioactive sources, namely, ^{60}Co, ^{241}Am-^{9}Be, and ^{239}Pu-^{13}C, and was linearly extrapolated to higher energies. The gain of the BaF_2 detectors was periodically monitored during the experiment and was found to be stable within ±1%. For each detector the pileup condition was generated from the individual E_{short} vs E_{long} spectrum. A typical TOF spectrum of the central BaF_2 detector is shown in Fig. 1 where the γ-prompt peak is clearly separated from the neutrons.

In the offline analysis, the events satisfying the following conditions were accepted: no pileup and γ prompt in BaF_2-TOF of the individual detectors and the prompt in T_{BGO}. The high-energy γ-ray spectra for individual detectors were generated in coincidence with fold for these selected events. Chance corrections for individual γ-ray spectra were done with appropriate gates in the BaF_2-TOF spectra. These chance-corrected individual γ-ray spectra were then calibrated and added. The Doppler correction was incorporated corresponding to a mean angle of 125° and for the average compound nucleus recoil velocity. From the two-dimensional matrix of fold and E_γ, different fold-gated experimental γ-ray spectra were projected. The high-energy γ-ray spectra for fold windows 8–9, 10–12, 13–15, and 16–36 are shown in Fig. 2.

It is important to estimate the contribution from trace low-Z impurities in the target, like C and O, if any. In particular, carbon buildup on the target surface during the experiment is of concern. While the actual concentration of trace impurities in the target could not be assessed in the present work, high-energy γ-ray spectra were recorded for identical beam conditions on a thin ^{12}C target for different folds. It was

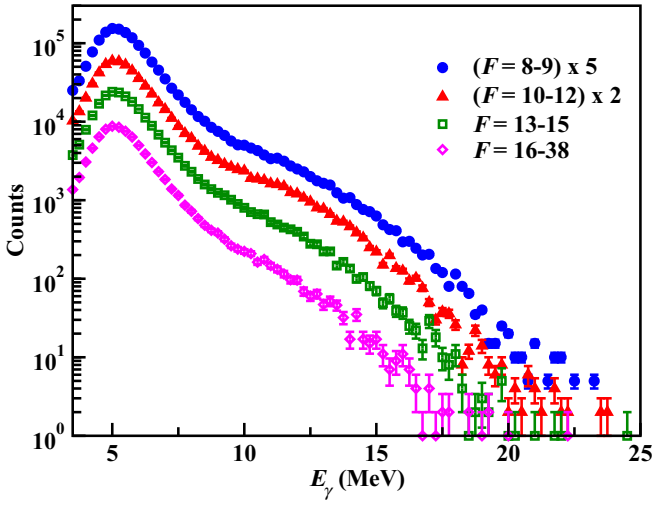

FIG. 2. High energy γ-ray spectra with different fold windows, suitably scaled for better viewing.

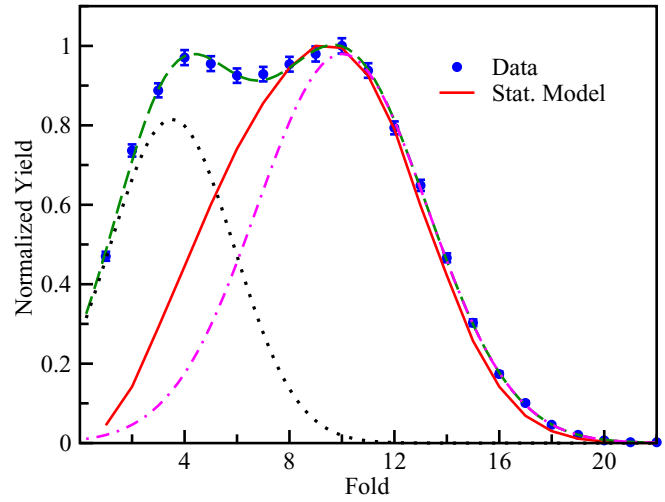

FIG. 3. The energy-gated (10–23 MeV) experimental fold distribution (blue dots) along with the statistical model fit (red line). The two-component Gaussian function fit is also shown (green dashed line) along with the individual components using black dotted and pink dash-dotted lines.

observed that the contribution to high-energy γ-ray spectra from carbon impurity for $F \geqslant 5$ was negligibly small. In addition, beam-induced background from the upstream and downstream beam line was checked periodically using a blank target frame and was also found to be negligible.

III. STATISTICAL MODEL ANALYSIS

The experimental fold-gated spectra are analyzed using a statistical model to extract the GDR parameters. A Simulated Monte Carlo CASCADE (SMCC) [20] code is used for this purpose. The excitation energy (E^*) of the CN was calculated from the projectile energy and the Q value of the reaction. The reduction in excitation energy due to pre-equilibrium particle emission [21] is expected to be negligible for a low value of $E^* \sim 71$ MeV and hence not taken into account. Similarly, because $E/A < 5$ MeV/nucleon, the nuclear bremsstrahlung contribution which is expected to be significant for $E/A > 8$ MeV/nucleon [22–24] is neglected in the present analysis. The angular momentum distribution of the CN is assumed to be of the following form:

$$\sigma(J_{\rm CN}) = \sigma_0 \frac{2J_{\rm CN}+1}{1+\exp[(J_{\rm CN}-J_0)/\delta J]}, \qquad (1)$$

with $\delta J = 2$. The level density prescription of Ignatyuk *et al.* [25] is used in all calculations with the asymptotic level density parameter $\tilde{a} = A/8.5$ MeV^{-1}. The parameters for the optical model potential for the calculation of transmission of neutrons, protons, and α particles were taken from Refs. [26–28]. In the SMCC code, the residue spin ($J_{\rm res}$) distribution is calculated as a function of E_γ by summing over all intermediate steps of γ decay for the full $J_{\rm CN}$ distribution. The multiplicity (M) of emitted γ rays was calculated using the relative probability (P_r) of $\Delta J_{\rm res} = 1$ and $\Delta J_{\rm res} = 2$ transitions from the state with spin $J_{\rm res}$ to ground state, which also took into account isomers in the residues. The multiplicity (M) to fold (F) response of the array depends on the efficiency and cross-talk probabilities, which are a function of E_γ. The response was obtained from simulations as described in Ref. [15]. The value of P_r was used as a parameter and was varied to reproduce the energy-gated ($E_\gamma = 10$ to 23 MeV) fold distribution. Figure 3 shows the experimental energy-gated fold distribution together with the statistical model fit using $P_r = 50\%$. There is a good agreement between the experimental and statistical model fold distribution for $F \geqslant 8$. The contribution at lower folds can arise from the fusion evaporation reactions with trace low-Z impurities present in the target (like C and O) and other noncompound processes. The experimental fold distribution can also be described as a sum of two Gaussians—one centered around $F \sim 4$ and the other around $F \sim 10$. This is plotted in the same figure to demonstrate that the contribution to $F \geqslant 8$ from the lower fold component is negligible. Hence, the data with $F \geqslant 8$ are used for extraction of the GDR parameters.

The search of the GDR parameters for the fold-gated γ-ray spectra in the windows $F = 8$–9, 10–12, 13–15, and 16–36 was carried out following the procedure described in Ref. [20]. The photoabsorption cross section for an axially symmetric deformed nucleus is given by [1]

$$\sigma_{\rm abs}(E_\gamma) = \frac{4\pi e^2\hbar}{mc}\frac{NZ}{A}\sum_{j=1}^{j=2}\frac{S_j\Gamma_j E_\gamma^2}{\left(E_\gamma^2 - E_j^2\right)^2 + E_\gamma^2\Gamma_j^2}, \qquad (2)$$

where N and Z are the neutron and proton numbers, and $E_{1(2)}$, $\Gamma_{1(2)}$, and $S_{1(2)}$ are the centroids, widths, and strengths for the two components, respectively. The calculated γ-ray spectra were folded with the response function of the BaF_2 array [15] and compared with experimental spectra. Both the calculated and experimental spectra were normalized at $E_\gamma = 8$ MeV,

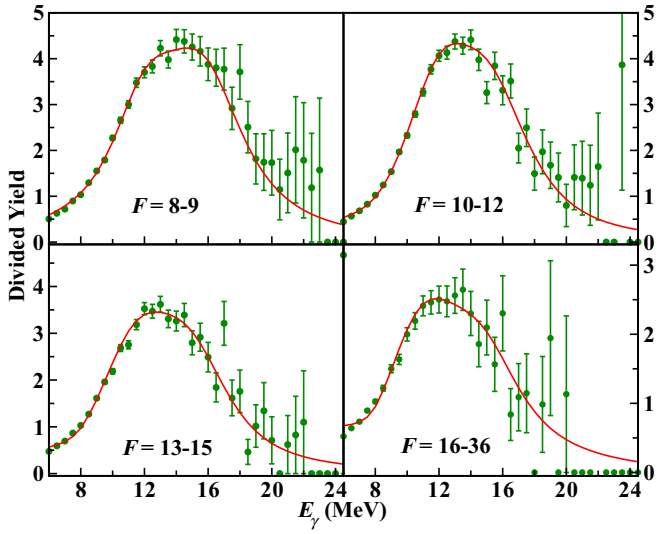

FIG. 4. Divided plots of experimental γ-ray spectra (green solid circled) and statistical model best fits (red line) with prolate deformation for different fold windows.

because the absolute GDR cross section was not measured in the present case. Because of this normalization procedure of the data with statistical model calculations, one assumes a fixed value of the Thomas-Reiche-Kuhn (TRK) sum rule and in all calculations the strength of the GDR is fixed at 100% (i.e., $S_1 + S_2 = 1$). It should be mentioned that the GDR parameters were also extracted for the $F = 10$–12 window by varying the total GDR strength at 75% and 125% of the TRK sum rule and are found to be the same within errors. The GDR centroid and width parameters were varied in fine steps (0.1 MeV) for both prolate ($S_1 : S_2 = 1 : 2$) and oblate ($S_1 : S_2 = 2 : 1$) deformation. For visualization of data on a linear scale, divided plots of the experimental as well as the calculated γ-ray spectra were generated for each fold window. A statistical model γ-ray spectrum calculated with an arbitrary constant $E1$

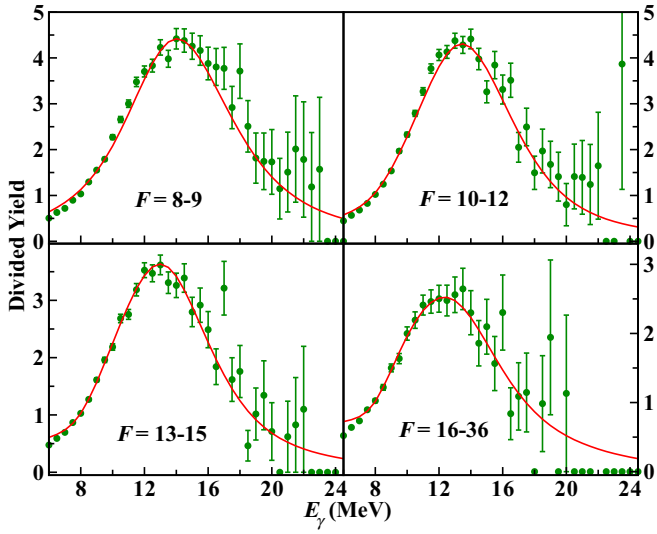

FIG. 5. Same as Fig. 4, but for the oblate deformed case.

TABLE I. Best-fit GDR parameters from SMCC analysis with prolate deformation for various fold windows.

Fold	E_1 (MeV)	Γ_1 (MeV)	E_2 (MeV)	Γ_2 (MeV)	S_2
8–9	12.8(1)	4.8(2)	16.5(2)	5.8(2)	0.67(2)
10–12	12.7(1)	4.6(2)	16.1(2)	6.2(2)	0.70(2)
13–15	12.5(1)	5.6(2)	16.0(2)	6.2(3)	0.70(2)
16–36	12.3(1)	5.9(2)	15.8(2)	6.0(3)	0.70(2)

strength of 0.2 W.u., folded with the BaF_2 detector response and normalized at 8 MeV, was used for generating divided plots. The goodness of the fit is achieved by χ^2 minimization and visual inspection of divided plots in the energy range 8–23 MeV.

Figure 4 shows the divided plots of the γ-ray spectra for different fold windows together with the best-fit statistical model spectra for prolate deformed case. Similar divided plots corresponding to oblate deformed case are shown in Fig. 5. It can be seen that the experimental data are described well in either case. The best-fit parameters for different fold windows obtained from the statistical model fits for prolate and oblate deformation are listed in Tables I and II, respectively. It should be mentioned that a single-component GDR fitting (corresponding to spherical shape) was also tried but was not successful in describing the data.

From the best-fit parameters for different folds, the GDR centroid energy E_D—weighted average of the centroid of two components and the effective GDR width (Γ_D)—the full width at half maximum of the total GDR strength function are obtained. The net excitation energy is taken as $U = E_f^* - E_{\rm rot} - \Delta_P$, where E_f^* is the excitation energy after the emission of the GDR photon, $E_{\rm rot}$ is the rotational energy, and Δ_P is the pairing energy, which is assumed to be independent of T and J. The temperature of the final state was calculated using the relation $U = aT_f^2$, where $a(U)$ is the level density parameter of Ignatyuk *et al.* [25]. The average values of the temperature ($\langle T \rangle$) and the angular momentum ($\langle J \rangle$) for each fold window are calculated using the same procedure followed in Ref. [15]. The J_f and T_f distributions following GDR γ-ray emission were calculated using the statistical model. The matrices $\sigma(J_f, F)$ and $\sigma(T_f, F)$ were generated after convoluting the $J_{\rm res}$ to F response and the average J and T values were extracted from the appropriate projections. The errors in temperature and angular momentum correspond to the FWHM of the respective distributions. It should be mentioned that uncertainties in $\langle T \rangle$ and $\langle J \rangle$, due to energy loss in the target, are much smaller compared to the width of these distributions.

TABLE II. Same as Table I, but for the oblate deformed case.

Fold	E_1 (MeV)	Γ_1 (MeV)	E_2 (MeV)	Γ_2 (MeV)	S_2
8–9	14.6(1)	7.2(2)	16.7(3)	8.0(3)	0.33(3)
10–12	14.2(1)	6.9(2)	16.5(3)	7.5(3)	0.33(3)
13–15	14.2(1)	7.0(2)	16.4(3)	7.8(4)	0.33(3)
16–36	14.1(1)	7.6(3)	16.0(3)	7.7(4)	0.33(3)

TABLE III. Extracted GDR parameters and nuclear deformation β, as a function of J and T for prolate deformation.

Fold	$\langle J\rangle$ ($\hbar$)	$\langle T\rangle$ (MeV)	E_D (MeV)	Γ_D (MeV)	β
8–9	26(9)	1.37(29)	15.3(2)	8.1(3)	0.30(2)
10–12	33(8)	1.33(28)	15.1(2)	8.1(3)	0.28(2)
13–15	38(7)	1.29(27)	15.0(2)	8.0(4)	0.29(2)
16–36	42(6)	1.25(26)	14.8(2)	7.8(4)	0.30(2)

IV. RESULTS AND DISCUSSION

The extracted GDR parameters, $\langle J\rangle$ and $\langle T\rangle$, corresponding to different fold windows are listed in Tables III and IV for prolate and oblate deformed cases, respectively. The deformation parameter (β) derived from the ratio of E_1 and E_2 [29] is also listed in the last column.

It may be emphasized that GDR parameters for ^{152}Gd from the present data and earlier measurements [6,15] are extracted in the same manner over a wide range of T and J.

A. Comparison with the PSF

To verify how well the present data compare with universal behavior (PSF) proposed by Kusnezov *et al.* [13], the reduced width $\Gamma_{\rm red}$ is calculated using the following equations:

$$\Gamma(T,J,A) = \Gamma(T,J=0,A)[L(\xi)]^{4/[(T/T_0)+3]}, \quad (3)$$

where

$$\Gamma(T,J=0,A) = \Gamma_0(A) + (6.45 - A/100)\ln(1+\mathrm{T/T_0}), \quad (4)$$

and the $\Gamma_{\rm red}$ is defined as

$$\begin{aligned}\Gamma_{\rm red} &= \Gamma(T,J,A)/\,\Gamma(T,J=0,A)\\ &= L(\xi), \quad \text{for } T = T_0\\ &\approx 1 + \frac{1.8}{1+e^{\frac{1.3-\xi}{0.2}}},\end{aligned} \quad (5)$$

where $\xi = J/A^{5/6}$ and $T_0 = 1.0$ MeV.

Figure 6 shows the reduced GDR width for the present data, for both prolate and oblate deformation, together with the scaling function (solid line) given by Eq. (5). The Γ_0 is taken as a parameter and fixed at 3.6 MeV. The data follow the universal behavior predicted by the PSF, indicating that the nuclei are in the liquid-drop regime. The $\Gamma_{\rm red}$ for $E^* \sim 87$ MeV data, calculated from the best-fit statistical model parameters

TABLE IV. Same as Table III, but for oblate deformation.

Fold	$\langle J\rangle$ ($\hbar$)	$\langle T\rangle$ (MeV)	E_D (MeV)	Γ_D (MeV)	β
8–9	26(9)	1.37(29)	15.3(3)	8.1(4)	0.19(2)
10–12	33(8)	1.33(28)	15.0(3)	8.0(4)	0.18(2)
13–15	38(7)	1.29(27)	14.9(3)	8.0(5)	0.17(2)
16–36	42(6)	1.25(26)	14.7(3)	8.3(5)	0.15(2)

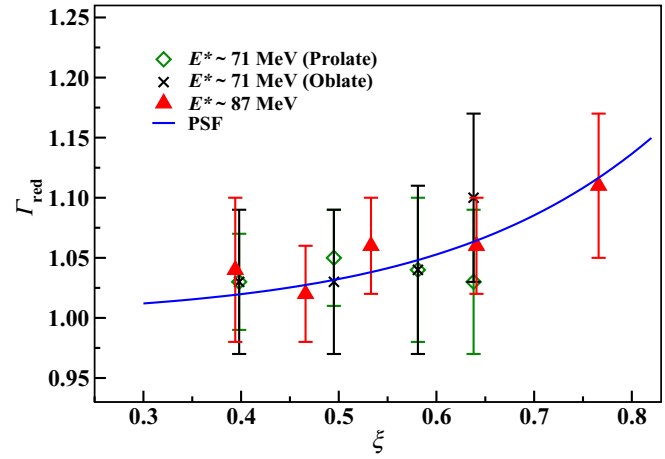

FIG. 6. The variation of reduced GDR width ($\Gamma_{\rm red}$) in ^{152}Gd as a function of $\xi = J/A^{5/6}$ with $\Gamma_0 = 3.6$ MeV, for $E^* \sim 71$ MeV (present data, for both prolate and oblate deformation) and for $E^* \sim 87$ MeV (data from Ref. [15]). The solid blue line represents the universal scaling given by Eq. (5).

given in Ref. [15], are also shown in the same figure for comparison (solid triangles). It should be pointed out that both these data sets are explained by the same $\Gamma_0 = 3.6$ MeV. This is consistent with the explanation in Ref. [6], where the influence of collisional damping at lower temperature is expected to be less significant.

B. Comparison with the TSFM

Theoretical calculations incorporating the thermal shape fluctuations in a numerically exact way [10] have been performed for the ^{152}Gd nucleus corresponding to the T-J range explored in the present experiment ($T = 1.25$ to 1.37 MeV and $J = 26\hbar$ to $42\hbar$). The average value of a GDR observable ($\mathcal{O}$) is calculated as

$$\langle\mathcal{O}\rangle_{\beta,\gamma} = \frac{\int_\beta\int_\gamma \mathcal{D}[\alpha]\exp[-F_{\rm TOT}(T,I;\beta,\gamma)/T]\Im_{\rm TOT}^{-3/2}\mathcal{O}}{\int_\beta\int_\gamma \mathcal{D}[\alpha]\exp[-F_{\rm TOT}(T,I;\beta,\gamma)/T]\Im_{\rm TOT}^{-3/2}}, \quad (6)$$

where $\mathcal{D}[\alpha] = \beta^4|\sin 3\gamma|\,d\beta\,d\gamma$ is the volume element and $\Im_{\rm TOT}$ represents the moment of inertia inclusive of shell and surface diffuseness corrections [10,30,31]. The free energy ($F_{\rm TOT}$) at fixed deformation (β,γ) is calculated using the finite temperature cranked Nilsson-Strutinsky method incorporating the T and J dependence of shell corrections [10,31]. The GDR cross section and nuclear shapes are related in a macroscopic model [10,32], where the response of the nucleus to the GDR γ rays is represented through an anisotropic harmonic oscillator with a separable dipole-dipole interaction. The corresponding Hamiltonian can be written as

$$H = H_{\rm osc} + \eta\, D^\dagger D, \quad (7)$$

where $H_{\rm osc}$ is the anisotropic harmonic oscillator Hamiltonian, and η and D represent the dipole-dipole interaction strength and the dipole operator, respectively. The parameter η is fitted to reproduce the observed GDR width for the ground state

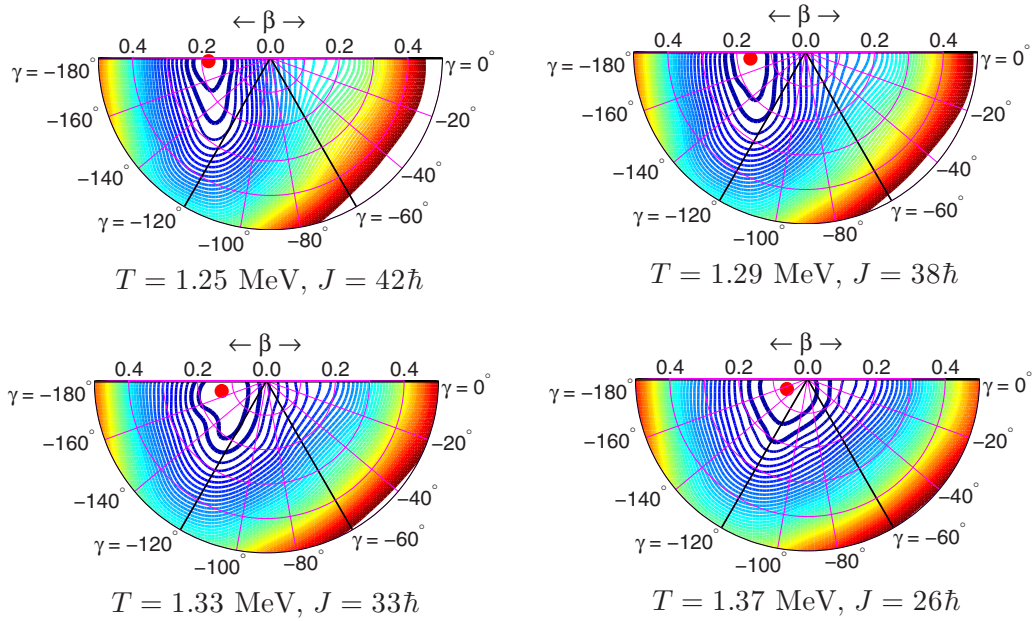

FIG. 7. Free energy surfaces of ^{152}Gd at different T and J combinations corresponding to the data at $E^* \sim 71$ MeV. In this convention, $\gamma = 0^\circ$ and -120° represent the noncollective and collective prolate shapes, respectively; $\gamma = -180^\circ$ and -60° represent the noncollective and collective oblate shapes, respectively. The contour line spacing is 0.2 MeV. The most probable shape is represented by a solid red circle and the first two minimum energy contours are indicated by thick lines.

of a given nucleus. Alternatively, it can be varied to fit the observed GDR cross sections or width at a given T. In the present calculation, η is taken to be 3.35.

The free energy surfaces at different T and J windows corresponding to the present data ($E^* \sim 71$ MeV) are presented in Fig. 7. As J increases, the most probable shape (MPS) of the nucleus, denoted by the red dot, also moves towards larger deformation. At $J = 26\hbar$, MPS has an axial deformation, $\beta < 0.1$ and $\gamma = -150^\circ$. At $J = 33\hbar$, the MPS corresponds to $\beta > 0.1$. At both these J values, the nucleus shows a clear γ softness spanning the region with $-180^\circ \leqslant \gamma \leqslant -120^\circ$. At $J = 38\hbar$ and $42\hbar$, the nucleus shows an oblate deformation with $\beta = 0.160$–0.190 and a crisp minimum. As T increases, the fluctuations also increase, which results in an increase in the GDR width. With increasing angular momentum, the axial deformation increases and could result in larger GDR width. However, at a fixed excitation energy, the angular momentum decreases with the increase in the temperature. The interplay between the role of T and J determines the final GDR width, which is dominated by T for lower J. The calculated values of β and the GDR width (Γ) in the measured T and J range, with and without thermal fluctuations, are listed in Table V. It is evident from the table that the effect of thermal fluctuations is significant, leading to an increase of Γ by more than 50%.

In principle, for comparison with data, the effect of fluctuations needs to be incorporated at all intermediate decay steps of the statistical model analysis [33,34]. Generally, the γ-ray cross section predicted by the TSFM ($\sigma_{\rm TSFM}$) is compared with the measured GDR cross section. The experimental GDR cross section is represented by the photoabsorption cross section used as input in the statistical model analysis. A comparison of $\sigma_{\rm TSFM}$ (red solid line) with the best-fit statistical model cross section ($\sigma_{\rm stat}$) for prolate and oblate deformation, are shown in Figs. 8 and 9, respectively. Because the absolute cross section is not measured in the present experiment, the integral of $\sigma_{\rm stat}$ was normalized to the total $\sigma_{\rm TSFM}$ in the $E_\gamma = 8$–23 MeV range. The variance in $\sigma_{\rm stat}$ shown in Figs. 8 and 9 is calculated from the errors on the best-fit parameters. It can be seen that the TSFM calculations describe the overall shape of the cross section very well in either case, but the statistical model fit for oblate deformation is in better agreement with the calculation. It should also be noted that $\Gamma_{\rm TSFM}$ values (see Table V) are somewhat larger ($\sim$4%–13%) than the measured GDR widths (see Tables III and IV). In Ref. [18] it was reported that the observed GDR widths in Refs. [6,15] could be fitted with $\eta = 3.35$, while the cross sections calculated with $\eta = 2.3$ compared well with the divided plot data. In the present work, with a proper representation of GDR cross sections, we observe that $\eta = 3.35$ describes both the cross sections and widths. Further, the large spread in the β values extracted from the

TABLE V. The calculated values of GDR widths and deformation parameters in TSFM with and without including thermal fluctuations.

		Without fluctuations		With fluctuations	
J ($\hbar$)	T (MeV)	β	Γ (MeV)	β	Γ (MeV)
26(9)	1.37(29)	0.060	5.2	0.318	8.4
33(8)	1.33(28)	0.130	5.8	0.320	8.6
38(7)	1.29(27)	0.160	6.0	0.320	8.7
42(6)	1.25(26)	0.190	6.2	0.324	8.8

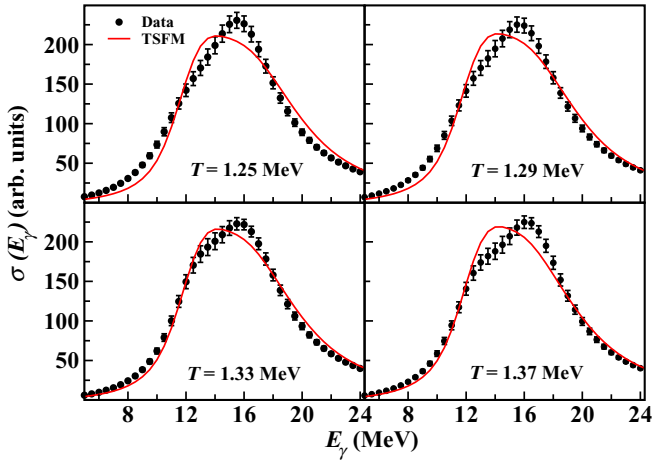

FIG. 8. The best-fit statistical model input cross section for prolate deformation (solid circle) and σ_{TSFM} with $\eta = 3.35$ (red line) for different fold windows.

statistical model analysis for prolate and oblate deformation also emphasizes the role of fluctuations.

C. Variation of GDR width with temperature

Combining the present data and earlier GDR measurements in ^{152}Gd [6,15], the variation of the GDR width (Γ) with temperature is shown in Fig. 10. The data span the range of $\langle J \rangle = 23\hbar$–$42\hbar$, which is $\leqslant J_C$ ($\sim 0.6A^{5/6}$ [13] $= 40\hbar$) and hence angular momentum is not expected to play a significant role.

It can be seen that the GDR width shows a small increase from $T \sim 1.2$ to 1.5 MeV. The data are compared with different scaling formulas and TSFM calculations. The top panel shows comparison with the phenomenological scaling formulas, PSF and CTF, while the TSFM calculations are shown in the bottom panel. Calculations are performed for $J = 20\hbar$ and $40\hbar$ in all three cases, corresponding to the J range of the data. The Γ_{PSF} is calculated using Eq. (3). The CTF calculations are done

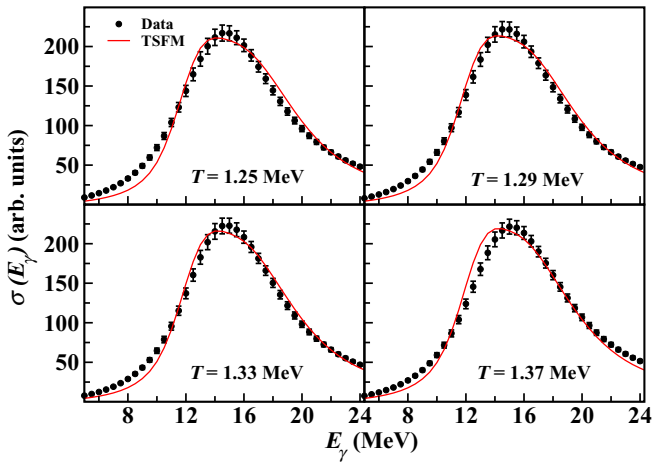

FIG. 9. Same as Fig. 8, but for oblate deformation.

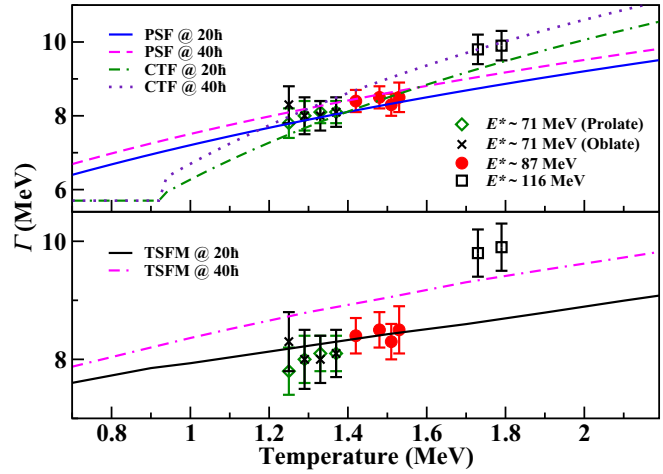

FIG. 10. Variation of the GDR width (Γ) as a function of temperature for ^{152}Gd and comparison with predictions of different models for $J = 20\hbar$ and $40\hbar$. The data for $E^* = 71$ MeV are from the present measurement and the data for $E^* = 87$ and 116 MeV are taken from Refs. [15] and [6], respectively. The data span the range of $\langle J \rangle = 23\hbar$–$42\hbar$. The top panel shows comparison with the PSF and the CTF, while TSFM calculations are shown in the bottom panel (see text for details).

using the formalism given in Ref. [17]:

$$\Gamma(T, J, A) = \Gamma(T, J = 0, A)[L(\xi)]^{7T_c/[T+3.3T_c]}, \quad (8)$$

where

$$\begin{aligned} \Gamma(T, J = 0, A) &= \Gamma_0(A), \quad \text{for} \quad T \leqslant T_c, \\ &= \Gamma_0(A) + c(A)\ln(T/T_c), \quad \text{for} \quad T > T_c, \end{aligned} \quad (9)$$

and

$$c(A) = 8.45 - A/50. \quad (10)$$

For ^{152}Gd, the critical temperature (T_c) = 0.92 MeV and $\Gamma_0(A) = 5.7$ MeV are taken from Ref. [17].

The PSF shows a very good agreement with the data for $T = 1.2$ to 1.5 MeV. The observed trend for this T range ($\sim$1.2 to 1.5 MeV) is also consistent with the TSFM prediction, while the Γ_{TSFM} values are about 4%–13% higher than the corresponding measured values. It can be seen that at higher temperature ($T \sim 1.8$ MeV) the experimental widths are larger than both the PSF and TSFM predictions, whereas the CTF calculations reproduce the observed trend as well as the measured widths over the $T \sim 1.2$ to 1.8 MeV range. More data on GDR width variation at $T \sim 1.0$ MeV and $T >$ 1.5 MeV would be useful to compare between these models and provide further insight into the temperature dependence of the GDR damping mechanism.

V. SUMMARY AND CONCLUSION

High-energy γ-ray spectra are measured in coincidence with low-energy discrete γ-ray multiplicity for the ^{152}Gd nucleus at an excitation energy of $\sim$71 MeV. The GDR parameters have been extracted for different T-J windows

using statistical model analysis. The observed variation of the GDR width follows the universal scaling law up to $J \sim 40\hbar$, as expected for the liquid-drop regime. Further, the reduced GDR width at $E^* \sim 71$ and 87 MeV can be consistently described by the PSF with $\Gamma_0 = 3.6$ MeV. It also implies that the contribution from other factors like collisional damping is less significant at lower temperatures ($T < 1.5$ MeV), as expected. The observed temperature variation of Γ also shows good agreement with the CTF. The GDR input cross sections extracted from the statistical model's best fit are compared with TSFM calculations and are found to be in good agreement, signifying the role played by fluctuations. The TSFM calculations predominantly favor the noncollective oblate shape, while the statistical model analysis with both prolate and oblate shapes describe the data. The present data together with earlier measurements indicate a slow variation of the GDR width for $T \sim 1.2$ to 1.5 MeV. This observed trend is well reproduced by the TSFM calculations, although the calculated values are ∼4%–13% higher than the data. GDR width studies at $T \sim 1.0$ MeV and $T > 1.5$ MeV would be useful to provide further insight into the GDR damping mechanism.

ACKNOWLEDGMENTS

The authors are grateful to Dr. D. R. Chakrabarty for help with the analysis programs and valuable discussions. We thank M. S. Pose, K. V. Divekar, and R. Kujur for their assistance during setup and the Pelletron Linac Facility staff for smooth operation of the accelerator. P.A. acknowledges the financial support from the Science and Engineering Research Board (India), SR/FTP/PS-086/2011 and DST/INT/POL/P-09/2014.

[1] K. A. Snover, Annu. Rev. Nucl. Part. Sci. **36**, 545 (1986).
[2] J. J. Gaardhøje, Annu. Rev. Nucl. Part. Sci. **42**, 483 (1992).
[3] A. Schiller and M. Thoennessen, At. Data Nucl. Data Tables **93**, 549 (2007).
[4] T. Baumann *et al.*, Nucl. Phys. A **635**, 428 (1998).
[5] P. Heckman *et al.*, Phys. Lett. B **555**, 43 (2003).
[6] D. R. Chakrabarty, V. M. Datar, S. Kumar, E. T. Mirgule, A. Mitra, V. Nanal, R. G. Pillay, and P. C. Rout, J. Phys. G: Nucl. Part. Phys. **37**, 055105 (2010).
[7] Ph. Chomaz, Phys. Lett. B **347**, 1 (1995).
[8] Y. Alhassid, B. Bush, and S. Levit, Phys. Rev. Lett. **61**, 1926 (1988).
[9] Y. Alhassid and B. Bush, Nucl. Phys. A **509**, 461 (1990).
[10] P. Arumugam, G. Shanmugam, and S. K. Patra, Phys. Rev. C **69**, 054313 (2004).
[11] M. Gallardo, M. Diebel, T. Døssing, and R. A. Broglia, Nucl. Phys. A **443**, 415 (1985).
[12] N. D. Dang, K. Tanabe, and A. Arima, Nucl. Phys. A **675**, 531 (2000).
[13] D. Kusnezov, Y. Alhassid, and K. A. Snover, Phys. Rev. Lett. **81**, 542 (1998).
[14] D. Pandit, S. Mukhopadhyay, S. Pal, A. De, and S. R. Banerjee, Phys. Lett. B **713**, 434 (2012).
[15] D. R. Chakrabarty, V. Nanal, V. M. Datar, S. Kumar, A. Mitra, E. T. Mirgule, and R. G. Pilllay, Nucl. Phys. A **770**, 126 (2006).
[16] D. R. Chakrabarty, Phys. Rev. C **74**, 017601 (2006).
[17] Deepak. Pandit, S. Bhattacharya, B. Dey, D. Mondal, S. Mukhopadhyay, S. Pal, A. De, and S. R. Banerjee, Phys. Rev. C **88**, 054327 (2013).
[18] A. K. Rhine Kumar and P. Arumugam, Phys. Rev. C **92**, 044314 (2015).
[19] http://www.tifr.res.in/∼pell/lamps.html.
[20] D. R. Chakrabarty, Nucl. Instrum. Methods Phys. Res., Sect. A **560**, 546 (2006).
[21] M. P. Kelly, K. A. Snover, J. P. S. van Schagen, M. Kicińska-Habior, and Z. Trznadel, Phys. Rev. Lett. **82**, 3404 (1999).
[22] H. Nifenecker and J. A. Pinston, Annu. Rev. Nucl. Part. Sci. **40**, 113 (1990).
[23] R. J. Vojtech, R. Butsch, V. M. Datar, M. G. Herman, R. L. McGrath, P. Paul, and M. Thoennessen, Phys. Rev. C **40**, R2441 (1989).
[24] C. A. Gossett, J. A. Behr, S. J. Luke, B. T. McLain, D. P. Rosenzweig, K. A. Snover, and W. T. Hering, Phys. Rev. C **42**, R1800 (1990).
[25] A. V. Ignatyuk, G. N. Smirenkin, and A. S. Tishin, Sov. J. Nucl. Phys. **21**, 255 (1975).
[26] D. Wilmore and P. E. Hodgson, Nucl. Phys. **55**, 673 (1964).
[27] F. G. Perey, Phys. Rev. **131**, 745 (1963).
[28] L. McFadden and G. R. Satchler, Nucl. Phys. **84**, 177 (1966).
[29] S. K. Rathi, D. R. Chakrabarty, V. M. Datar, S. Kumar, E. T. Mirgule, A. Mitra, V. Nanal, and H. H. Oza, Phys. Rev. C **67**, 024603 (2003).
[30] P. Arumugam, A. Ganga Deb, and S. K. Patra, Europhys. Lett. **70**, 313 (2005).
[31] P. Arumugam, A. Ganga Deb, and S. K. Patra, Eur. Phys. J. A **25**, 199 (2005).
[32] G. Shanmugam and M. Thiagasundaram, Phys. Rev. C **37**, 853 (1988).
[33] O. Wieland *et al.*, Phys. Rev. Lett. **97**, 012501 (2006).
[34] M. Ciemała *et al.*, Phys. Rev. C **91**, 054313 (2015).